Flight Performance Evaluation of the Flying-V

de Zoeten, G.J.; Varriale, Carmine; Vos, Roelof

DOI
10.2514/6.2023-3484

Publication date
2023

Document Version
Final published version

Published in
AIAA AVIATION 2023 Forum

Flight Performance Evaluation of the Flying-V

Godert J. de Zoeten*, Carmine Varriale†, Roelof Vos‡
Delft University of Technology, Delft, 2629 HS, The Netherlands

This study evaluates the flight performance of a Flying-V aircraft designed for transonic passenger transport. The Flying-V is a disruptive aircraft configuration that has shown to possess promising aerodynamic performance during preliminary design. It is compared to a competitor aircraft reminiscent of the Airbus A350-1000, for the same thrust-to-weight ratio and a similar number of passengers. The most common performance metrics for the take-off, landing, climbing and cruise phases have been assessed using a modular flight mechanics model. Take-off and landing performance are evaluated through flight simulation using a simple Euler method, while climb and cruise performance are evaluated in trimmed, steady-state conditions. Only instantaneous performance is available for the latter two phases. The Flying-V outperforms its competitor for basically all investigated metrics. Take-off length is shorter, mainly due to a larger tail strike attitude that reduces the minimum unstick speed. Service and absolute ceiling are higher, and its superior lift-over-drag ratio results in a 21% increase in the cruise range parameter. Landing field lengths are similar for both aircraft, but the Flying-V has a significantly larger pitch angle during approach. This causes longer de-rotation length, and a large obscured segment of the pilot's vision which could be problematic during operations.

List of symbols

α	angle of attack, rad
β	angle of sideslip, rad
γ	flight path angle, rad
δ	control surface deflection, rad
δ_T	normalized throttle
η	overall power plant efficiency
θ	pitch angle, rad
μ	friction coefficient
Λ	sweep angle, deg
Θ	ambient temperature ratio w.r.t sea level
a	speed of sound, m/s
b	reference span, m
c	mean aerodynamic chord, m
g	gravitational acceleration, m/s^2
h	altitude, m
p, q, r	roll, pitch, yaw rate, rad/s
t/c	thickness over chord ratio
x	longitudinal position, m
$\mathcal{AR}$	aspect ratio
D	aerodynamic drag, N
J_{ii}	moment or product of inertia, kg·m^2
H	calorific value of fuel, J/kg
L	aerodynamic lift, N
M	Mach number
N	number of elements
RP	range parameter
S	reference area, m^2
SAR	specific air range, m/kg
T	thrust, N
$TSFC$	thrust-specific fuel consumption, g/(N·s)
V	airspeed, m/s
W	weight, N

Subscripts and superscripts

app	approach
cs	control surface
dd	drag divergence
lo	lift-off
mg	main landing gear
mu	minimum unstick
ng	nose landing gear
pax	passengers
sl	sea level
ts	tail-strike

I. Introduction

Over the course of the last 50 years, the overall efficiency of the tube-and-wing aircraft configuration has improved by 100 percent [1]. But the progress in terms of efficiency gains has slowed over the course of time, and the conventional

*MSc Student, Flight Performance and Propulsion Section, Faculty of Aerospace Engineering
†Assistant Professor, Flight Performance and Propulsion Section, Faculty of Aerospace Engineering, C.Varriale@tudelft.nl; AIAA Member.
‡Associate Professor, Flight Performance and Propulsion Section, Faculty of Aerospace Engineering, R.Vos@tudelft.nl; AIAA Member.

aircraft configuration is regarded to be approaching an asymptote in terms of overall efficiency with the Airbus A350 and Boeing 787 [2]. With the demand for air travel doubling approximately every 15 years [3] and increasing constraints in terms of noise and pollution, engineers have started looking at unconventional aircraft configurations that are possibly more fuel efficient than the conventional configuration.

The Flying-V is a tailless, V-shaped aircraft in which the passenger cabin is integrated in each wing. It was first proposed in 2015 by Benad [4], and is shown in Figure 1. Designed for the same mission as the Airbus A350, the Flying-V has a lower wetted-area-to-volume ratio, a higher effective span due to the tall winglets, and a lower structural mass due to the lateral distribution of the payload. A three-member family of Flying-V airplanes has been designed where constant-cross-section wing plugs are employed to extend or shrink the wing and cabin [5]. Compared to the A350-1000, the Flying-V-1000 has shown a 15% reduction in maximum take-off mass and a 22% reduction in fuel burn over a 15 400 km range with a payload mass of 67 metric tonnes. This is in line with the earlier findings that showed the potential of a 25% improvement in aerodynamic efficiency along with a 15% reduction in the FEM-mass-to-takeoff-mass ratio[2, 6].

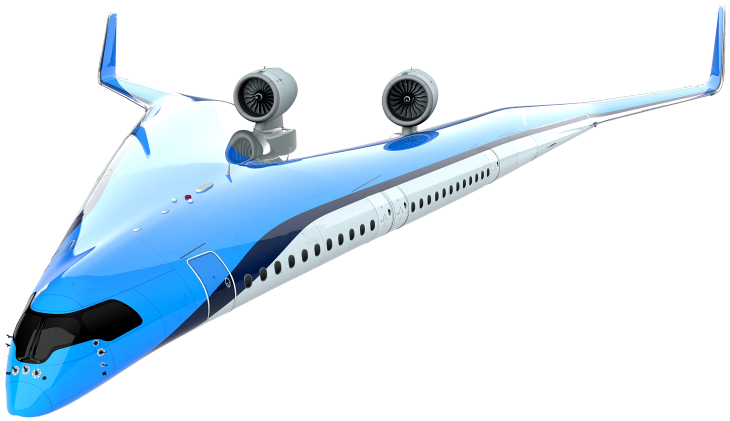

Fig. 1 Rendering of the Flying-V aircraft.

While these studies showed promising results in terms of energy efficiency, they also sparked many research questions. One line of research has concentrated on the control and handling qualities of the airplane. A 4.6%-scale flight-test article was designed and built to measure the dynamic properties of the airplane. A half-model of the same size was first experimentally examined in the wind tunnel. Based on wind tunnel tests, Palermo and Vos [7] showed that the sub-scale model develops a strong pitch-up moment above an angle of attack of 20 deg. Viet showed that the highly swept wing develops a complicated vortex pattern that changes with the angle of attack [8]. Subsequent aerodynamic analysis using large-eddy simulations revealed that both the pitch break and the vortex formation are sensitive to the flight Reynolds number, and are suppressed to angles of attack in excess of 30 deg.

To derive the aerodynamic model of the sub-scale airplane, system identification techniques were applied to the wind tunnel experiments as well as the flight tests, with excellent correlation between the two [9, 10]. These tests showed that the airplane is naturally stable in all modes. This confirmed the findings of a separate study performed by Cappuyns, who numerically evaluated the handling qualities of the full-scale Flying-V using a vortex-lattice model to represent the aerodynamic behavior of the model [11]. This model was subsequently used in experiments in a flight simulator to score the handling qualities on a Cooper-Harper rating [12, 13]. These studies demonstrated that the Flying-V has Level 1 handling qualities across the majority of the flight envelope.

In this paper, the flight performance of the Flying-V is compared to the one of the Airbus A350. The overall research question that is answered is: how does the flight performance of the Flying-V compare to the Airbus A350, provided both airplanes have an identical thrust-to-weight ratio? The overall flight performance comprises four different parts: landing performance, take-off performance, climb performance and cruise performance. For each of these parts, appropriate metrics are defined to compare the flight performance aspects. A flight mechanics analysis is employed to simulate the performance of either airplane during each of these flight phases. Both newly generated data and data from earlier studies are used to populate the various models that underpin the flight mechanics analysis.

The remainder of the is paper is structured as follows. Section II presents the disciplinary models that function as a basis for the flight mechanics model: the reference geometries, aerodynamics, propulsive units, contact forces and

landing gear, and mass distribution. Then, section III presents how the various flight maneuvers have been modelled and evaluated within the context of a simple flight simulation framework. In section IV, the predictions of the flight mechanics model for the landing and take-off performance of the Airbus A350 are compared to the corresponding data available in the open literature. The evaluation of the flight performance of the Flying-V, with comparison to the A350, is subsequently presented in section V. Lastly, section VI presents the conclusions of this study and provides possible avenues for further research.

II. Flight mechanics model

This section presents the flight mechanics model employed to analyze the flight performance of both aircraft under investigations: the Flying-V-1000 and the Airbus A350-1000. The following subsections describe each aspect of the overall flight mechanics model in more detail. The top-level architecture of the complete model is presented in Figure 2.

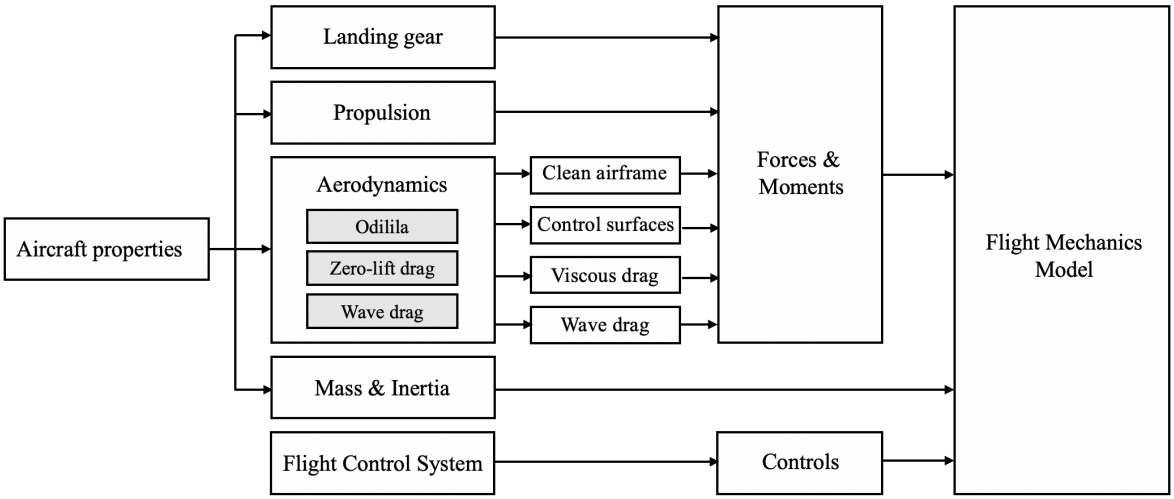

Fig. 2 Block-scheme of the flight mechanics model employed for both aircraft under investigation.

Table 1 shows the input specifications that have been used for this comparison study. The Flying-V-1000 has been designed for a similar passenger capacity and Payload Mass (PLM) as the A350-1000. In light of its unconventional geometry, it is able to obtain an 18% reduction in Maximum Take-off Mass (MTOM) with respect to its competitor, as found by a previous study on the Flying-V family [5]. According to another study on the structural characteristics of the Flying-V, its Operating Empty Mass (OEM) is about 32% lower than the competitor [6]. The fraction between the Maximum Landing Mass (MLM) and the MTOM of the Flying-V has been assumed to be the same as the one of the A350-1000. Moreover, the thrust-to-weight ratio of both aircraft has also been assumed to be the equal for both aircraft. With these assumptions, it is expected that the flight performance differences that are to be found can be attributed exclusively to the difference in aerodynamic characteristics and mass properties.

Table 1 Top-level specifications for both aircraft under investigation.

	Flying-V-1000 [5, 6]	Airbus A350-1000 [14, 15]
N_{pax}	361	366
PLM	67 000 kg	67 000 kg
MTOM	259 000 kg	316 000 kg
MLM	193 000 kg	236 000 kg
T_{max}	707 kN	863 kN
T/W	0.278	0.278

A. Geometry

The wing planform of the Flying-V-1000 as designed by Oosterom [5] and the one of the Airbus A350-900 have been used to generate the aerodynamic datasets necessary for flight simulation. A planform comparison between the two reference models is shown in Figure 3a. Figure 3b shows the position and role of all movable devices employed for each aircraft.

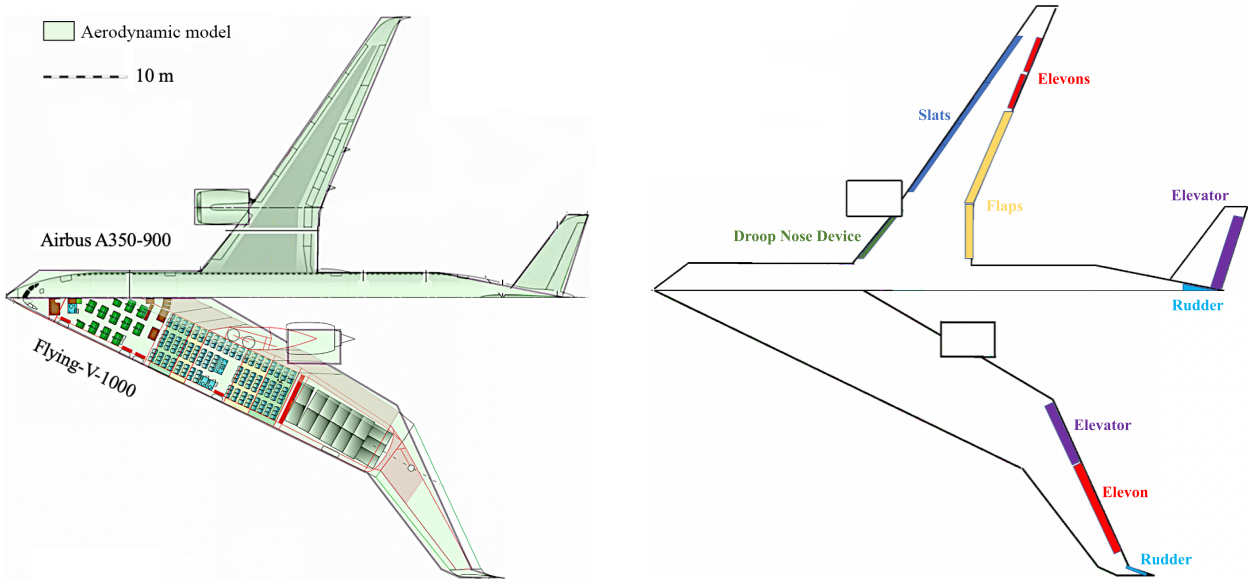

a) Planform comparison

b) Control surfaces positions and sizes

Fig. 3 Comparison among reference plan forms of the Airbus A350-900 and Flying-V-1000, with control location and role of movable devices.

Since the aerodynamic dataset is generated by a Vortex Lattice Method (VLM), as illustrated in the following section, it is deemed acceptable to use the A350-900 reference geometry to derive a dataset for the A350-1000. The two aircraft employ the same main wing and empennage, but the A350-1000 has a slightly larger winglet than the -900 version. The moment arm of the empennage with respect to the center of gravity has been increased by 6.98 m to take into account the extra fuselage length of the A350-1000. Similarly, the reference point for the reduction of all moments has been shifted backwards by 3.81 m to account for the different position of the wing.

Over-the-wing spoilers, not reported in the figures, are assumed to be employed exclusively for breaking on the runway. In this phase, the deflection of spoilers increases both the aerodynamic drag and the down-force on the main landing gear. As the latter increases, the maximum braking force that can be applied without skidding also increases, hence allowing for a further reduction of the required braking distance to standstill on the runway. The landing gear dimensions of the Flying-V have been obtained from [16], using the "Floor 5.5" configuration. The corresponding pitch angles for tail-strike have also been retained for this study. The top-level geometric characteristics of the two aircraft have been reported in Table 2.

B. Aerodynamics

Aerodynamic actions and derivatives due to the airframe and movable devices are expressed as a function of the angle of attack α and asymptotic Mach number M, and are linearly proportional to the angle of sideslip β, body angular rates p, q, r and control surface deflections $\boldsymbol{\delta}$. Such baseline aerodynamic model is expressed in Equation 1 for a generic action (force or moment) coefficient C_F. All actions are expressed in body axes through data tables which are interpolated linearly at run-time.

$$C_F(\alpha, M, \beta, \omega, \delta_{\text{cs}}) = C_{F_0}(\alpha, M) + \frac{\partial C_F(\alpha, M)}{\partial \beta}\beta + \sum_{\omega=p,q,r} \frac{\partial C_F(\alpha, M)}{\partial \omega}\omega + \sum_{i=1}^{N_{\text{cs}}} \frac{\partial C_F(\alpha, M)}{\partial \delta_i}\delta_i \tag{1}$$

For the dataset of the A350, the C_{F_0} term contains aerodynamic actions due to the airframe in take-off, landing and cruise configurations. The Flying-V does not incorporate high-lift devices.

Table 2 Top-level geometric characteristics of both aircraft under investigation.

Parameter	Flying-V-1000	Airbus A350-1000
b	65 m	65 m
S	883 m^2	462 m^2
$\mathcal{AR}$	4.78	9.15
c	18.74 m	9.48 m
$\overline{\Lambda}_{c/4}$	55.8 deg	29.6 deg
$\overline{t/c}$	0.1299	0.1036
θ_{ts}	19.2 deg	10.0 deg
x_{mg}	31.8 m	37.1 m
x_{ng}	6.47 m	4.63 m

The numerical database underlying such model has been generated using the Odilila VLM. This software has been developed by Airbus, and its predictions of lift curve slopes and induced drag have been verified in previous research studies [6, 11]. As all VLMs, Odilila assumes incompressible, inviscid and irrotational flow, and is therefore inherently limited. Thickness and viscosity effects are also absent, together with non-linear aerodynamic behaviors. These limitations justify the adoption of a slightly inaccurate geometry, as mentioned in the previous section, but also necessitate awareness in the modeling and interpretation of certain performance.

In order to avoid operating in a non-linear aerodynamic regime, a maximum usable angle of attack of $\alpha_{\text{max}} = 20\,\text{deg}$ has been imposed for all flight simulations of the Flying-V, in light of the pitch-up break tendencies that have been discovered through wind tunnel experiments [7]. For the A350-1000, such limit has been instead assumed to be 15 deg.

To account for thickness, viscosity and interference effects, the baseline aerodynamic dataset from Odilila has been enhanced with a semi-empirical, component-based zero-lift drag model [17, 18]. For the wings, fuselage, nacelles and pylons, the zero-lift drag coefficient is calculated using the flat plate skin-friction coefficient C_f, a form factor f to account for wave drag, an interference factor Q and the wetted area of the component S_{wet}, according to Equation 2.

$$C_{D_0} = C_f f Q_c \frac{S_{\text{wet}}}{S} \tag{2}$$

Estimated zero-lift drag contributions in take-off, touch-down and cruise conditions are reported in Table 3a. Figure 4 shows the aerodynamic efficiency and lift curves of the Flying-V and Airbus A350 in subsonic and transonic regimes.

In the event of an engine failure, the additional drag due to a blocked rotor or windmilling engine are also modelled using empirical relations [18]. It is assumed that the zero-lift drag does not contribute to the aerodynamic moments about the aircraft Center of Gravity (CG), except for in the case of the failed engine and the landing gear. For the latter, separate strut and wheel drag coefficients have been determined, and drag forces are assumed to be applied at the middle of the strut and at the centre of the wheel, respectively. Moment contributions due to these drag forces are calculated and added to the external aerodynamic moments, after appropriate transformation to the body reference frame.

An empirical model based on the "Delta Method" has been implemented to account for transonic wave drag [19, 20]. As shown in Equation 3, the three-dimensional drag divergence number $M_{\text{dd}}^{\text{3D}}$ has been estimated for both aircraft on the basis of its two-dimensional counterpart $M_{\text{dd}}^{\text{2D}}$, depending on airfoil characteristics, and corrected for quarter-chord sweep angle and aspect ratio of the wing.

$$M_{\text{dd}}^{\text{3D}} = M_{\text{dd}}^{\text{2D}} + \Delta M_{\Lambda_{c/4}} + \Delta M_{\mathcal{AR}} \tag{3}$$

The average quarter-chord sweep angle and thickness-to-chord ratio presented in Table 2 have been used for the wave drag computations. The resulting three-dimensional drag divergence number are reported in Table 3b. The Flying-V has a larger $M_{\text{dd}}^{\text{3D}}$ than its competitor due to the benefits of a large sweep angle and a small aspect ratio. Although the Delta method data includes a wide range of aircraft with sweep angles up to 60 degrees and aspect ratios as low as 4.7, it must be noted that none of the investigated aircraft was a flying wing. Therefore it is not known whether this method could also be accurately applied to this unconventional aircraft configuration. For the A350-1000 the fuselage wave drag has also been accounted for, although its contribution is small.

The deflections of over-the-wing spoilers are assumed to have only effect on the change in lift coefficient, while their effect on drag has been neglected. This is to avoid giving the Flying-V an unfair advantage when comparing braking performance, since its model for drag due to spoilers needs to be further verified. For the Flying-V, it is assumed that the change in lift coefficient due to spoiler deflection is $\Delta C_L = -0.16$, on the basis of previous research [21]. For the Airbus

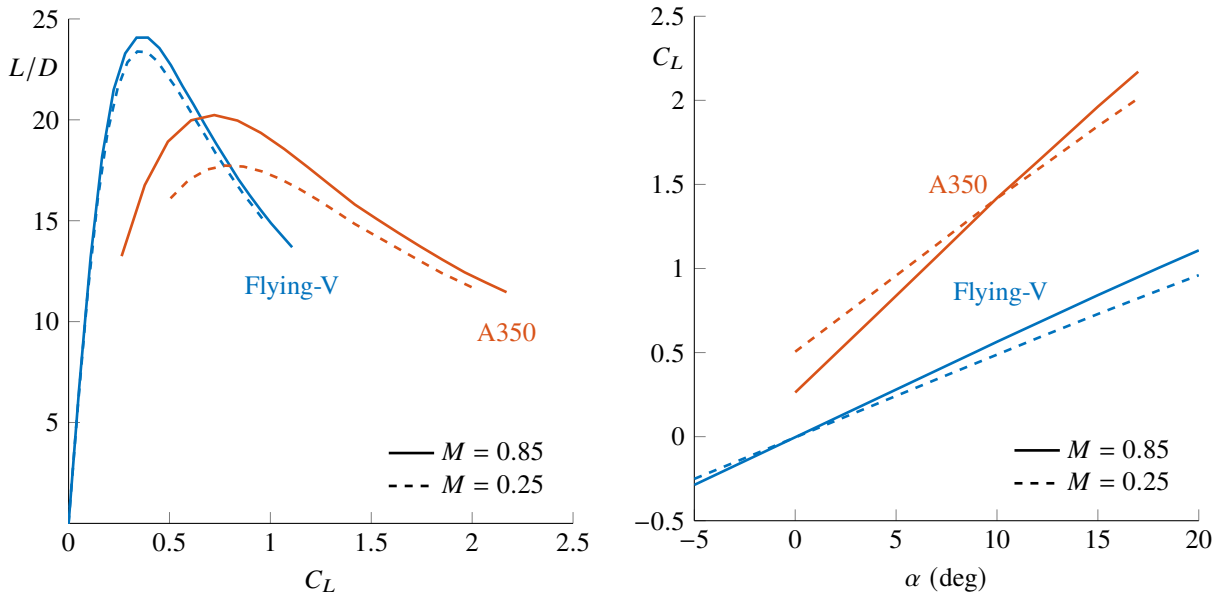

a) Lift over drag ratio

b) Lift curve

Fig. 4 Clean aerodynamics of the Flying-V-1000 and Airbus A350-1000 in subsonic and transonic regimes. All drag contributions included. All movable devices and landing gear retracted.

Table 3 Corrections to the baseline aerodynamic dataset based on semi-empirical models.

(a) Zero-lift drag coefficient per component in various flight phases

ΔC_{D_0} Component	Flying-V-1000			Airbus A350-1000		
	Take-off	Landing	Cruise	Take-off	Landing	Cruise
Fuselage	-	-	-	48.9	50.5	46.1
Wings	62.9	64.0	61.2	94.9	99.6	89.4
Nacelles	6.5	6.6	6.3	14.2	14.9	13.4
Pylons	3.5	3.5	3.4	5.3	5.5	5.0
Leakage	4.4	4.4	4.4	8.0	8.0	8.0
Flaps	-	-	-	68.5	205.4	-
Landing gear	50.5	50.5	-	80.0	80.0	-

(b) Maximum angle of attack, drag-divergence Mach number, and ΔC_L due to over-the-wing spoiler deflections

	Flying-V-1000	Airbus A350-1000
α_{max}	20 deg	15 deg
M_{dd}^{3D}	0.961	0.867
ΔC_L	−0.16	$-0.13 - 0.34(\delta_{flap}/30)$

A350-1000, it is a function of the flap deflection angle: $\Delta C_L = -0.13 - 0.34(\delta_{\text{flap}}/30)$. The latter model has been formulated on the basis of available data from the Boeing 747. This is deemed acceptable, since force coefficients are normalized with respect to the wing reference area, and the planform of the A350-1000 and B747 are overall comparable at the fidelity level adopted for this study.

C. Propulsion

Both the Flying-V and the reference aircraft employ two high-Bypass Ratio (BPR) engines, comparable to the Rolls Royce Trent XWB [14]. The engines locations have been taken from [22] and [14] for the Flying-V and Airbus A350, respectively. A semi-empirical thrust lapse model based on engine data of two-shaft turbofan engines is used to predict the available thrust and *TSFC* for different altitudes, Mach numbers, and flight phases [23]. Such model is shown in Figure 5a for a turbofan engine with BPR = 10 and a Static Sea-Level (SSL) thrust equal to $T_{\text{SSL}} = 353\,\text{kN}$.

In the present work, the model for maximum available thrust during take-off is going to be used for flight conditions at $M < 0.4$ and $h < 1\,\text{km}$. In all other flight conditions, the thrust lapse for the climb phase is used. The resulting maximum available thrust predicted by this merged model as a fraction of the SSL thrust is shown in Figure 5b.

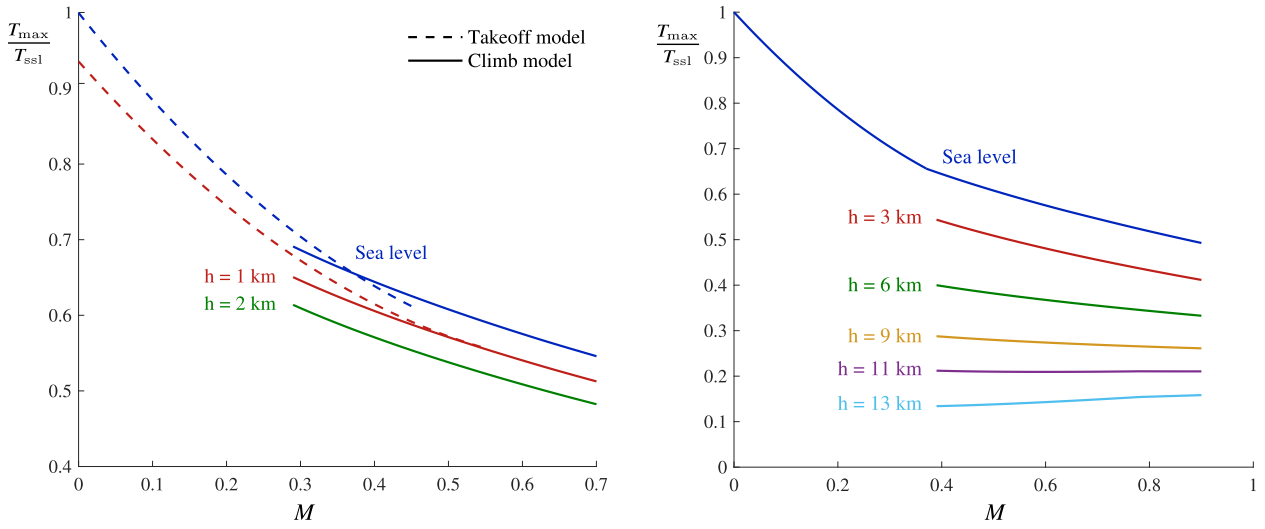

a) Thrust lapse models for take-off and climb phases

b) Merged thrust lapse model

Fig. 5 Maximum available thrust as a fraction of the SSL thrust as a function of Mach number and altitude, for a turbofan engine with BPR = 10 and $T_{\text{SSL}} = 353\,\text{kN}$.

The specific fuel consumption is calculated as a function of altitude and Mach number using the following Equation 4,

$$TSFC = TSFC_{\text{ref}} \sqrt{\frac{\Theta}{\Theta_{\text{ref}}}} \left(\frac{M}{M_{\text{ref}}} \right)^n \tag{4}$$

where Θ is the ambient temperature ratio with respect to sea level temperature [23]. The reference *TSFC*, temperature ratio and Mach number are the respective values in cruise conditions. The same reference values have been chosen for both aircraft. A value of $TSFC_{\text{ref}} = 13.5\,\text{g}/(\text{kN}\cdot\text{s})$ is assumed, which corresponds to the one of the Airbus A350-1000 [24]. The reference Mach number is assumed to be 0.85, and the reference altitude 11 km. The exponent n is engine-specific, and has been estimated to be equal to 0.42 [23].

The overall power plant efficiency is expressed as in the following Equation 5 [25], where H is the calorific value of the fuel. The latter has been assumed to be equal to $43.2\,\text{MJ}/\text{kg}$ for both aircraft.

$$\eta = \frac{a_{\text{sl}}}{H/g} \frac{M}{TSFC/\sqrt{\Theta}} \tag{5}$$

D. Contact forces

Contact between the runway and each landing gear is established on the basis of the current position and attitude of the aircraft. When the wheels of either the main or nose landing gear make contact with the runway, two additional

types of forces are modeled: a reaction force normal to the runway, and a friction force parallel to the runway. The friction force is parallel to the runway and proportional to the normal force through a friction coefficient μ.

Only longitudinal-symmetric flight is considered in all flight phases involving ground contact forces. During ground contact, it is assumed that the contact forces between the runway and the landing gear wheels are able to counteract excess yawing and rolling moments, as well as side forces. The normal reaction forces and the friction forces are calculated at every time-step by assuming that the aircraft is instantaneously in static equilibrium. Actions due to inertial accelerations are therefore neglected. This is an important limitation of the chosen approach for the absolute estimation of the performance of each aircraft, but the comparison between the two aircraft performance remains fair.

Braking is modelled by simply adjusting the friction coefficient of the wheels of the main landing gear. The rolling friction coefficient is assumed to be $\mu_{\text{mg}} = 0.02$ for a dry concrete runway [26]. When brakes are applied, a braking coefficient is assumed to be constant and equal to $\mu_{\text{mg}} = 0.4$ [21].

E. Inertia and Center of Gravity

The inertia tensor used in the present research has been estimated through a structural analysis of the Flying-V-1000 and A350-900 [6]. The moments of inertia of the Airbus A350-1000 have then been estimated by correcting the A350-900 values for the mass and geometric differences between the -900 and -1000 models. Aircraft mass is assumed to be distributed symmetrically about the x-axis, hence the J_{xy} and J_{yz} products of inertia are assumed to be zero. The J_{xz} product is neglected, as it can be expected to be very small compared to the principal moments of inertia. Numerical values for both aircraft are presented in Table 4a.

The range of CG locations that can be used by the Flying-V has also been found in previous research [11]. The foremost CG location is the one that allows to obtain a load factor of $1.3g$ with a pull-up maneuver in approach conditions. The aftmost CG location was determined by imposing a static margin of 2.5%. For the Airbus A350-1000, the CG limits are taken from the corresponding Aircraft Characteristics and Maintenance Planning (ACAP) manuals [14]. The usable CG range of both aircraft is reported in Table 4b, in terms of the Mean Aerodynamic Chord (MAC).

Table 4 Moments of inertia and CG limits of both aircraft under investigation.

(a) Moments of inertia around the aircraft body principal axes.

	Flying-V-1000		Airbus A350-1000	
	MTOM	OEM	MTOM	OEM
$J_{xx}/10^6\,\text{kg}\cdot\text{m}^2$	39.6	12.2	31.8	9.4
$J_{yy}/10^6\,\text{kg}\cdot\text{m}^2$	27.6	10.5	50.8	28.2
$J_{zz}/10^6\,\text{kg}\cdot\text{m}^2$	65.8	21.4	86.4	37.4

(b) Usable CG range for stability and controllability

	Flying-V-1000	Airbus A350-1000
x_c^{le}	20.94 m	31.75 m
$x_{\text{CG}}^{\text{fore}}$	$0.45c$	$0.18c$
$x_{\text{CG}}^{\text{aft}}$	$0.57c$	$0.43c$
Δx_{CG}	$0.12c$	$0.25c$

III. Methodology

The Performance, Handling Qualities and Load Analysis Toolbox (PHALANX) has been used to integrate an aerodynamic, a weight and balance, and a propulsion module into a complete flight mechanics model, which can be employed to perform 6-Degree of Freedom (DoF) flight simulation. The toolbox has been developed in-house in MATLAB, using the Simulink and Simscape multi-body dynamics packages. It has already been implemented in several other research applications to unconventional aircraft configurations [27, 28], including studies on the propulsive empennage concept [29], and the trim and transient response of staggered box-wing aircraft [30, 31]. A top-level overview of the PHALANX flight simulation toolbox is shown in Figure 6.

The following subsections present in more detail the methodology adopted to simulate flight dynamics and calculate flight performance, and illustrate the approach adopted to model different flight phases.

A. Flight dynamics simulation

Flight dynamics is simulated by summing the force and moment contributions due to the airframe aerodynamics, the propulsion system, ground contact forces, and inertial loads in the aircraft body reference frame. These contributions depend on model states as well as on the control inputs provided by a pre-implemented pilot model, and/or calculated

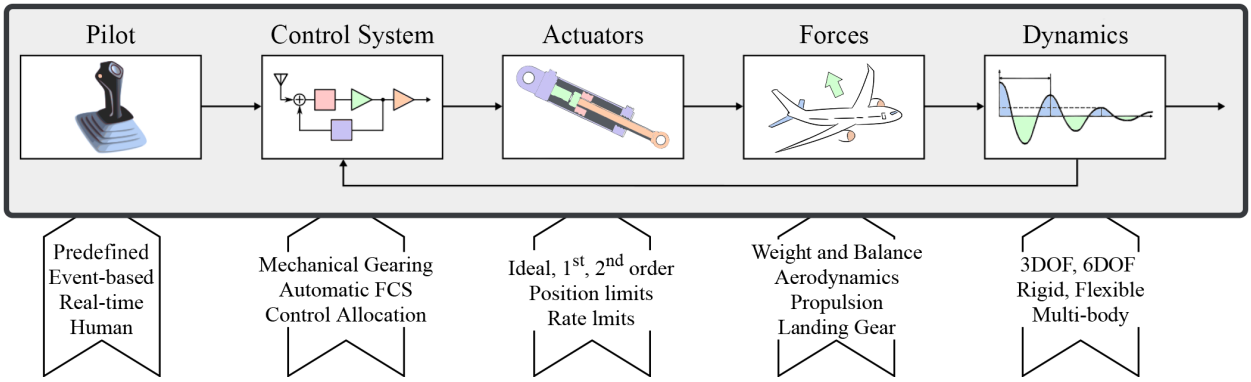

Fig. 6 Top-level overview of the PHALANX flight simulation toolbox.

through a simple FCS (FCS). State propagation is achieved, in this particular study, through a forward Euler scheme. The angle of attack and angle of sideslip are calculated at each time-step from the airspeed components in body axes.

The aircraft is trimmed by prescribing initial values of altitude, airspeed, sideslip angle and Euler angular rates. Either the flight path angle γ or the throttle level δ_T can be additionally specified to further constrain the formulation of the trim problem. Trim is achieved by finding the combination of pilot inputs on the stick and Euler angles that minimize the norm of an array containing the aircraft linear and angular accelerations, together with the error in the prescribed sideslip angle. If trim is required for a longitudinal-symmetric flight condition, the pilot inputs on the lateral-directional axes, as well as the roll and yaw attitude angles are automatically set to zero, and the trim problem is greatly simplified. In all cases, the solution is found with an iterative, gradient-based optimization algorithm, and is therefore locally optimum [31].

The FCS involves an open-loop pilot model and the possibility to implement different types of closed-loop controllers. Movable surfaces are controlled by (auto-)pilot inputs for the roll, pitch and yaw axes, and the throttle setting δ_T. Actuators are assumed to be ideal, with a deflection limit of 30 deg. With reference to Figure 3b, the A350 employs the elevator for pitch control, the rudder for yaw control and the elevons exclusively for roll control. The Flying-V employs both the elevon and elevator for pitch control, while the elevon and rudder are used for roll and yaw control, respectively. Different PID controllers are implemented to perform certain maneuvers, as explained briefly in the following sections.

B. Take-off

The take-off maneuver begins at standstill and ends when the lowest point of the aircraft surpasses the screen height $h_{\text{screen}} = 35$ ft [32]. The maneuver is simulated using 2D equations of motion, restricting the evolution of the aircraft to be symmetric in the vertical plane. The runway is assumed to be horizontal ($\gamma = 0$). The aircraft uses its maximum available thrust at full throttle ($\delta_T = 1$), and each engine spools up/down with a characteristic time of 5.0 s.

The aircraft initiates rotation about the contact point of the main landing at a certain speed V_{R}. The optimal value of V_{R} is determined for a given aircraft model via an iterative search algorithm with an accuracy of 0.5 m/s. During the first part of the rotation phase, a reference pitch rate q_{ref} is targeted, until the angle of attack reaches an assigned value α_{ref}. This value is assigned arbitrarily to minimize overshoot in the following part of the rotation phase. Once α_{ref} has been reached, a reference pitch angle θ_{ref} is targeted. The reference value is assigned for each aircraft model on the basis of the tail-strike angle, reported in Table 2: $\alpha_{\text{ref}} = \theta_{\text{ts}} - 0.5$ deg.

If One Engine Inoperative (OEI) conditions occur before the decision speed V_1, the take-off procedure is aborted. In such a scenario, the following operations are simulated:

1) 2.9 s after the engine failure, the friction coefficient of the main landing gear is updated to its braking value;
2) 3.3 s after the engine failure, the failed engine is cut-off from the FCS;
3) 4.3 s after the engine failure, over-the-wing spoilers are fully deployed to act as speed bakes.

The aforementioned time delays have been introduced to take into account typical human behavior during the corresponding operations [33]. An additional controller deflects control surfaces over the main wing to maximize the loading on the main landing gear while retaining at least 8% of the aircraft weight on the nose wheel. This is in order to allow the pilot to maintain directional control of the aircraft [17, 18].

If the OEI condition occurs after the decision speed V_1, the take-off procedure is continued. In such a case, as soon as the nose wheel loses contact with the ground, an automatic controller calculates the rudder deflection required to neutralize the yawing moment due to thrust imbalance. Such deflection is used exclusively to account for its additional aerodynamic drag, but every other force and moment is disregarded. In other words, it is assumed that the aircraft is always able to maintain its straight trajectory on the runway. On the other hand, it can be expected that the predicted take-off distance in OEI conditions are slightly underestimated, since the airborne phase does not include sideslipping flight or a banking angle.

C. Landing

Like for the take-off maneuver, landing is simulated using 2D equations of motion, and only longitudinal-symmetric flight is considered. The landing maneuver begins with the aircraft being trimmed at a screen height of 50 ft, with a flight path angle $\gamma = -3\,\text{deg}$, at an assigned approach speed V_{app}. The approach speed is assumed to be equal to 1.23 times the stall speed in landing configuration [32]. It has been calculated using the available aerodynamic model at SSL and MLM conditions. For the Flying-V, $V_{\text{app}} = 74.6\,\text{m/s}$, while for the A350, $V_{\text{app}} = 75.6\,\text{m/s}$

Until the aircraft altitude is greater than 1 m above ground, a simple autopilot uses the elevators to target a reference touch-down descent rate equal to $1.83\,\text{m/s}$, which is the recommended outcome of a standard flare maneuver [32]. For the two aircraft under investigation, this value corresponds to a flight path angle approximately equal to $\gamma_{\text{ref}} = -1.4\,\text{deg}$. Additionally, engine thrust is reduced to idle, while taking the aforementioned spool time into account.

After touching down, de-rotation is initiated by targeting a reference pitch rate $q_{\text{ref}} = -3\,\text{deg/s}$. Once the nose-wheel contacts the runway, braking is simulated by updating the value of the friction coefficient of the main gear, deploying the over-the-wing spoilers as speed brakes, and deflecting control surfaces to maximize the load on the main landing gear. This procedure is identical to the one described in the previous III.B for an aborted take-off.

D. In flight phases

During the climb and cruise phases, the 3D equations of motion are used to trim the aircraft in different flight conditions. No dynamic simulation is performed in these flight phases, hence the estimated performance should be interpreted as quasi-steady. Asymmetric flight conditions and non-zero side-slip angles are also considered in case of OEI conditions. The landing gear is assumed to be retracted, and all its contributions are therefore null.

For the cruise phase, attention is focused on the maximum Specific Air Range (*SAR*). *SAR* is the range covered per unit of fuel consumed, and is defined in the following Equation 6, where η is the overall power plant efficiency, introduced in Equation 5.

$$SAR = \frac{V}{T \cdot TSFC} = \frac{H}{g}\frac{1}{W}\eta\frac{L}{D} \tag{6}$$

The instantaneous *SAR* is inversely proportional to the aircraft weight and, in the most general case, directly proportional to the Range Parameter *RP*, defined in the following Equation 7. In light of the expression of η and the chosen model for *TSFC*, this parameter is proportional to the product between the aerodynamic efficiency and the Mach number elevated to a power lower than one. This choice results in the fact that no propulsive parameter has any impact on the cruise performance evaluation.

$$RP = \eta\frac{L}{D} \propto M^{1-n}\frac{L}{D} \tag{7}$$

Alternatively, if *TSFC* was to be assumed to be constant across the flight envelope, the *RP* would be proportional to the transonic efficiency ML/D [25]. If the overall efficiency η was assumed to be constant altogether, the range parameter would be simply proportional to the aerodynamic efficiency L/D.

IV. Validation

To validate the fidelity of the overall flight mechanics model and adequacy of the developed methodology, the predicted take-off and landing distances of the A350-1000 are compared to reference data extracted from the ACAP report [14].

A series of landing simulations have been performed for the A350-1000 model, in SSL conditions, at MLM with different positions of the CG. The resulting landing field lengths range from 2112 m to 2153 m, and have been compared to a reference landing distance of approximately 2100 m. The latter has been calculated by dividing the measured landing distance provided in the ACAP report by 0.6, as prescribed by the Federal Aviation Regulations [34].

A series of take-off simulations have been performed for different aircraft weights and at different altitudes. The reference values reported in the ACAP model have been assumed to be equal to 115% of the measured take-off distance, as prescribed by Certification Specifications [32]. Hence, the measured take-off lengths from simulations have been scaled up accordingly. The comparison between the estimated runway lengths and the updated reference values is shown in Figure 7. The flight mechanics model seems able to predict take-off runway lengths reasonably well for altitudes up to about 610 m, while the calculated runway lengths seems to be under-predicted at altitudes of approximately 1220 m.

Despite limited, the validation process is regarded as satisfactory. The results are believed to be sufficiently accurate to justify the use of the developed flight mechanics model and methodology for the purpose of comparing the performance of the A350-1000 and Flying-V-1000 aircraft models.

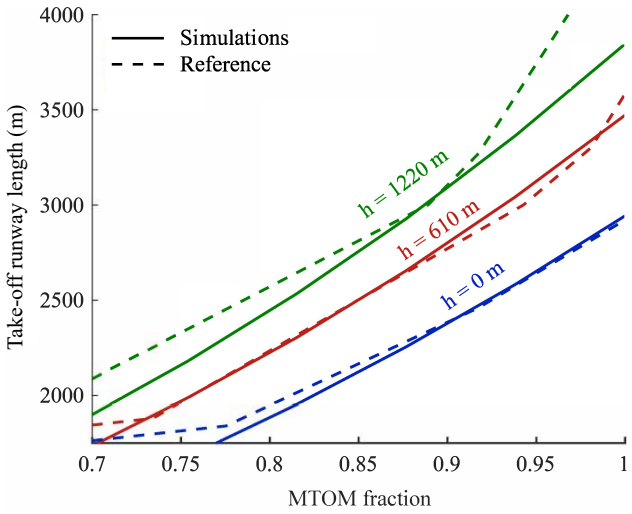

Fig. 7 Validation of take-off runway length for the A350-1000 with reference data extracted from the ACAP [14].

V. Results

This section presents the flight performance of the Flying-V-1000, with comparison to the one of the Airbus A350-1000. Classic performance metrics related to the four main mission phases of take-off, landing, climb and cruise are presented and discussed in the corresponding sub-sections.

A. Take-off performance

In accordance with CS25.113, the take-off distance has been calculated as 115% of the horizontal distance along the take-off path, with all engines operative, from standstill to the point where the aircraft is 35 ft above the runway [32]. The minimum take-off distance of both aircraft is reported in Figure 8a for different altitudes and MTOM fractions, and with the CG at its forward limit position. On average, the Flying-V-1000 achieves a take-off distance 25% shorter than the A350-1000, with such difference increasing with increasing mass and altitude. This is to be attributed to the fact that the the Flying-V-1000 has:

- a lower absolute MTOM than its competitor (Table 1);
- a much larger reference area, despite a lower lift-slope, which allows it to obtain comparable lift to its competitor, for a given angle of attack (Table 2, Figure 4b);
- a much larger tail-strike attitude, which allows it to achieve greater angles of attack during the ground run (Table 2);

These three conditions result in the minimum unstick speed V_{mu} of the Flying-V-1000 being significantly lower than for the A350-1000, as shown in Figure 8b.

The take-off distance breakdown of the two aircraft is compared in Figure 9, for different CG positions, at SSL and MTOM. For both aircraft, the total take-off distance decreases as the CG shifts rearwards. This is mainly due to a

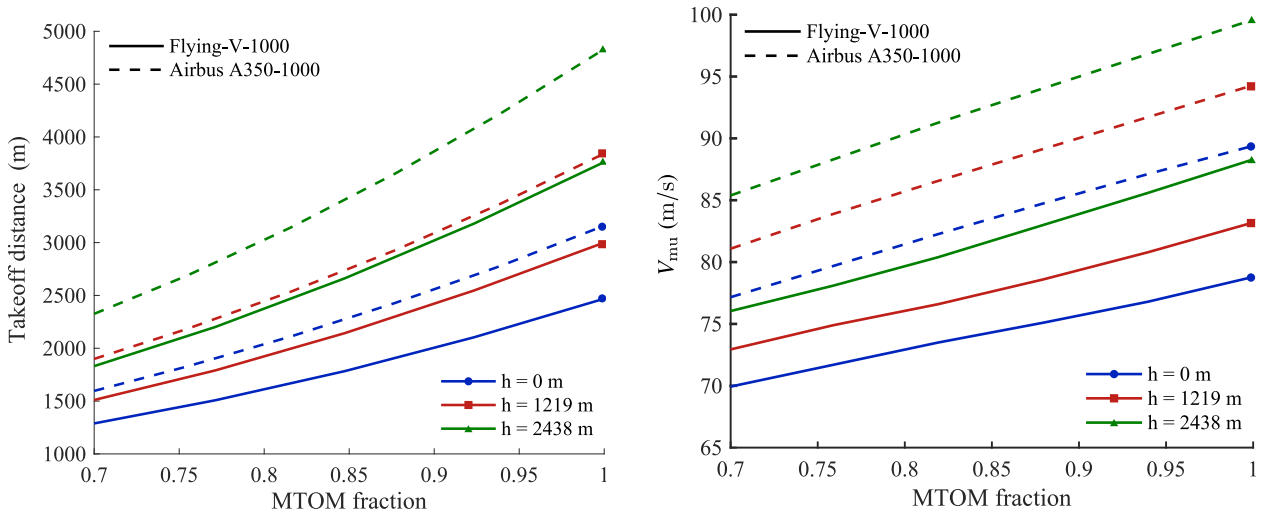

a) Takeoff distance **b)** Minimum unstick speed

Fig. 8 Minimum take-off distance and corresponding minimum unstick speed of the Flying-V-1000 and the Airbus A350-1000, for different altitudes and MTOM fractions. CG is at the respective forward limit position for each aircraft.

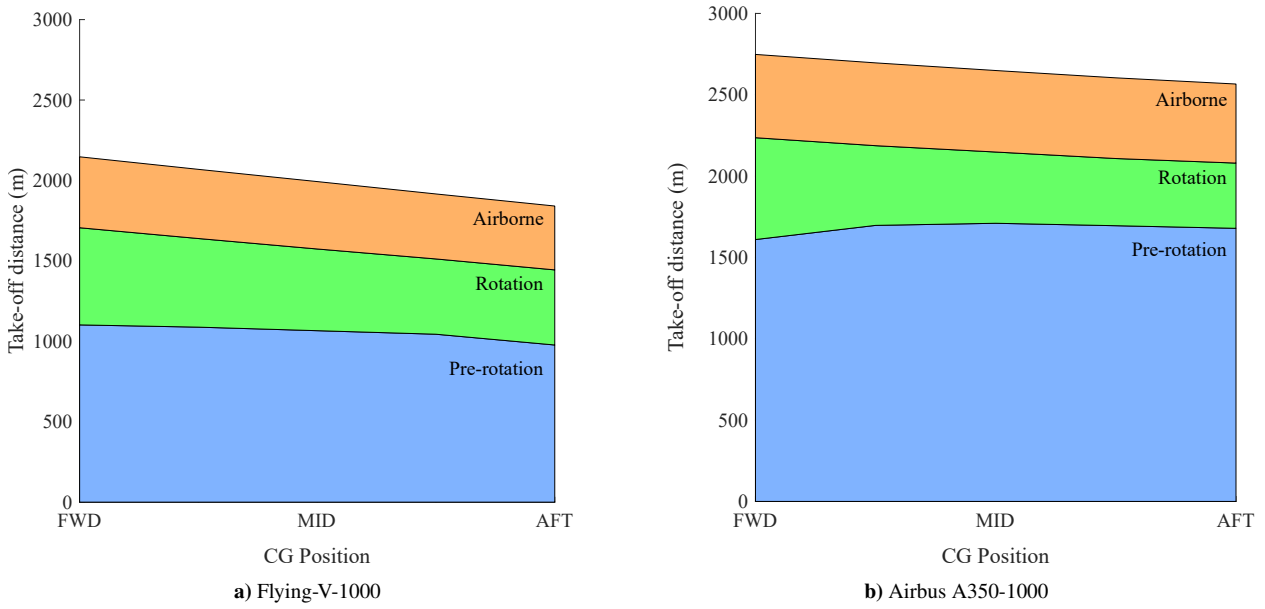

a) Flying-V-1000 **b)** Airbus A350-1000

Fig. 9 Take-off distance breakdown comparison between the Flying-V-1000 and A350-1000, for varying CG positions, at SSL and MTOM.

decrease in distance during the rotation phase. The Flying-V-1000 features a larger decrease in take-off distance over the entire CG range, indicating that the CG position has a larger influence on the optimal V_R for the Flying-V-1000 than for the A350-1000. This could be expected, since the CG range of the Flying-V-1000 is closer to the longitudinal position of the main landing gear.

In particular, the most rearward CG position of the Flying-V almost coincides with the position of the main landing gear, while the most rearward CG position of the A350-1000 lies about 1.3 m ahead of its main landing gear. Since the moment arm of the aircraft weight with respect to the main landing gear is much smaller for the Flying-V-1000 than for the A350-1000, it is possible to rotate the nose of the aircraft upwards at an earlier speed for the former. On the other hand, the absolute distance covered during the rotation phase is lower for the A350-1000, on average. This is mostly due to the fact that the rotation phase starts at a higher speed for the latter. Finally, the airborne distance of the Flying-V-1000 is shorter for all CG positions. This is due to a lower lift-off speed, and a larger climb angle at lift-off as

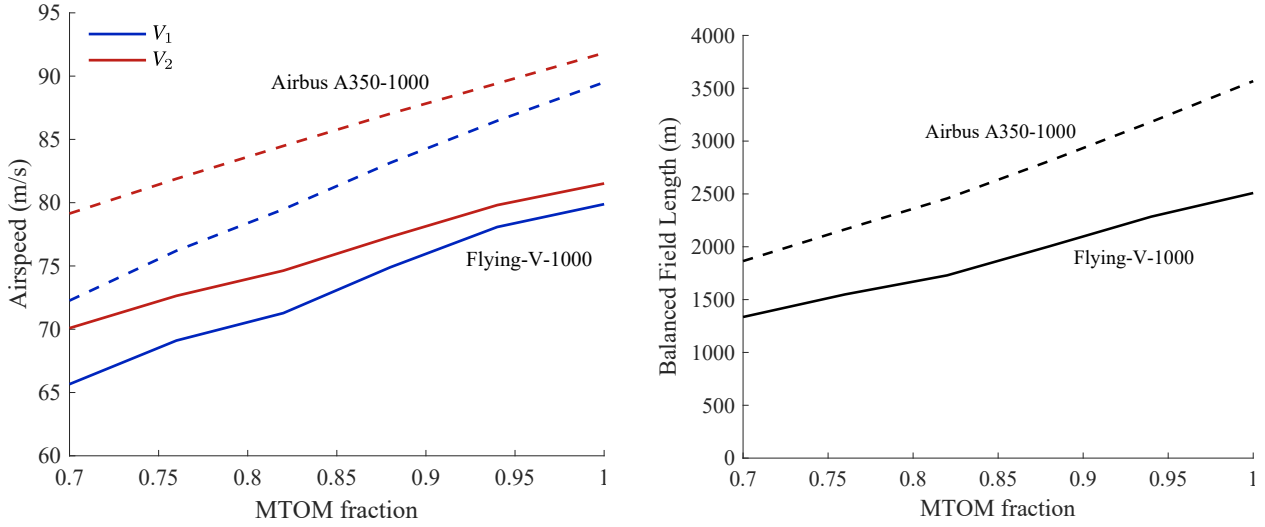

a) Decision and take-off speeds

b) Balanced Field Length (BFL)

Fig. 10 Performance parameters of the Flying-V-1000 and the Airbus A350-1000 for the OEI take-off maneuver, for different MTOM fractions. CG at forward limit in SSL conditions.

compared to the A350-1000.

Figure 10 compares the main performance parameters related to a take-off maneuver in OEI conditions. All of the reported parameters are found by simulating the failure of an engine at an assigned speed during the ground run, and simulating both a continued take-off and an aborted take-off after such event. The decision speed V_1 and the take-off speed V_2 at the screen height are found when the distances for continued and aborted take-off are equal. By definition, such distance is the Balanced Field Length (BFL).

The figure shows that both the reference speeds and the BFL of the the Flying-V-1000 are significantly lower than the ones of the A350-1000. This is mostly caused to the different position of the engines within each aircraft. Due to the over-the-wing position of the engines for the Flying-V, an engine failure results in a pitch-up tendency of the aircraft with respect to the all-engines-operative condition. It is then easier to initiate rotation with OEI for the Flying-V-1000 rather than for the A350, with its engines installed under the wing. Lastly, the decision and take-off speeds uniformly decrease by about 2–2.5% when shifting the CG to its rearward limit position. The same occurs for the BFL.

B. Landing performance

A comparison between the landing distance breakdown of the Flying-V-1000 and A350-1000 is shown in Figure 11. The two aircraft have comparable total landing distance for all positions of the CG, but a different repartition of distance covered in the three main phases of the landing maneuver. During the airborne phase, the A350-1000 covers a slightly larger distance than the Flying-V-1000. This is due to the slightly higher approach speed of the A350, which additionally requires a more extended flare maneuver to reduce the descent rate at touchdown.

During the de-rotation phase, the A350 covers much less distance than the Flying-V. This is because the latter has a higher pitch attitude at touchdown and a lower pitch attitude when resting on the ground ($\theta = -3$ deg), and the maneuver is simulated with the same imposed de-rotation pitch rate for both aircraft. For both aircraft it can be seen that the de-rotation distance decreases as the CG shifts rearwards, since this determines a lower pitch attitude at touchdown. For the Flying-V-1000 this effect has a larger impact on the landing distance than for the A350-1000.

In the braking phase, the Flying-V requires a much shorter distance until standstill than the A350. This is ascribable to the fact that it is able to generate a much grater aerodynamic load on the main lading gear, and can be justified by two factors. Firstly, the Flying-V-1000 has no high-lift devices and a ground attitude of $\theta = -3$ deg. On the runway ($\gamma = 0$), this results in the airframe naturally generating down-force on the main landing gear. Secondly, despite both aircraft use spoilers for lift dumping, the Flying-V is able to deflect all of its trailing-edge control surfaces, as opposed to only the tail elevator of the A350. The time history of the total load on the main landing gear during landing is reported in Figure 12a, while the time history of the aircraft deceleration is shown in Figure 12b.

Due to its highly swept wing and the absence of high lift systems, the Flying-V-1000 requires a larger landing pitch

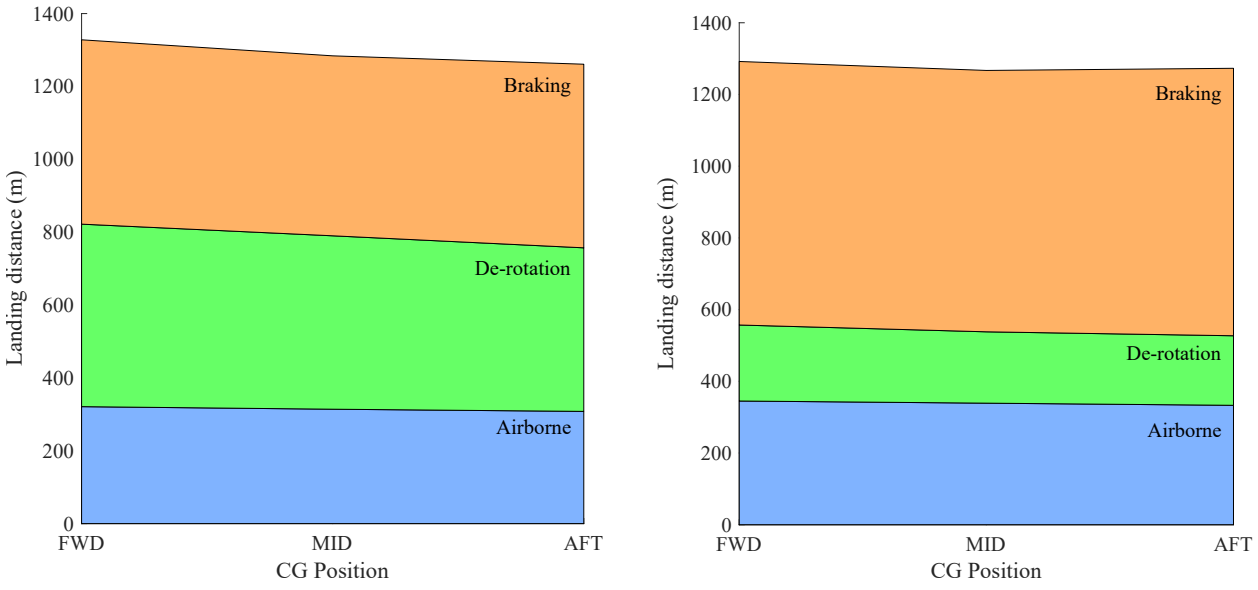

a) Flying-V-1000 **b)** Airbus A350-1000

Fig. 11 Landing distance breakdown comparison between the Flying-V-1000 and A350-1000, for varying CG positions, at SSL and MLM.

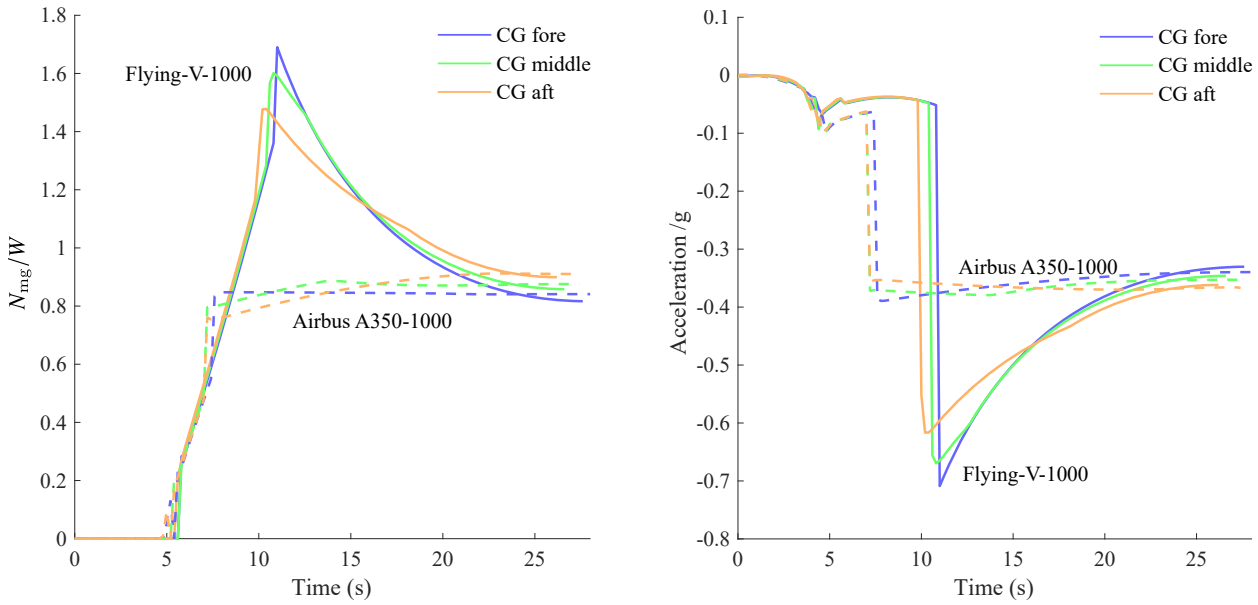

a) Total load on the main landing gear **b)** Aircraft deceleration

Fig. 12 Time histories comparison of total load on the main gear wheels and aircraft deceleration during landing, for different positions of the CG.

angle than the A350-1000. Time histories of the pitch angle of both aircraft during landing are shown in Figure 13a. During the flare maneuver, the pitch angle is increased even more to reduce the descent rate, and this may become problematic for the pilots to have a clear view of the runway. Figure 13b shows the time history of the obscured segment during landing. This is the horizontal distance to the closest point on the ground that the pilot can see, in light of the aircraft attitude and nose geometry [35]. The pilot's eye is assumed to be located 1.87 m behind the nose and 1.00 m above the aircraft centre line, while the over-nose angle of the cockpit is assumed to be 25.7 deg for the Flying-V-1000 and 20 deg for the A350-1000 [14]. For both aircraft, it can be seen that the landing pitch attitude increases when the CG is shifted forward, which also results in a significantly larger obscured segment. The obscured segment of the

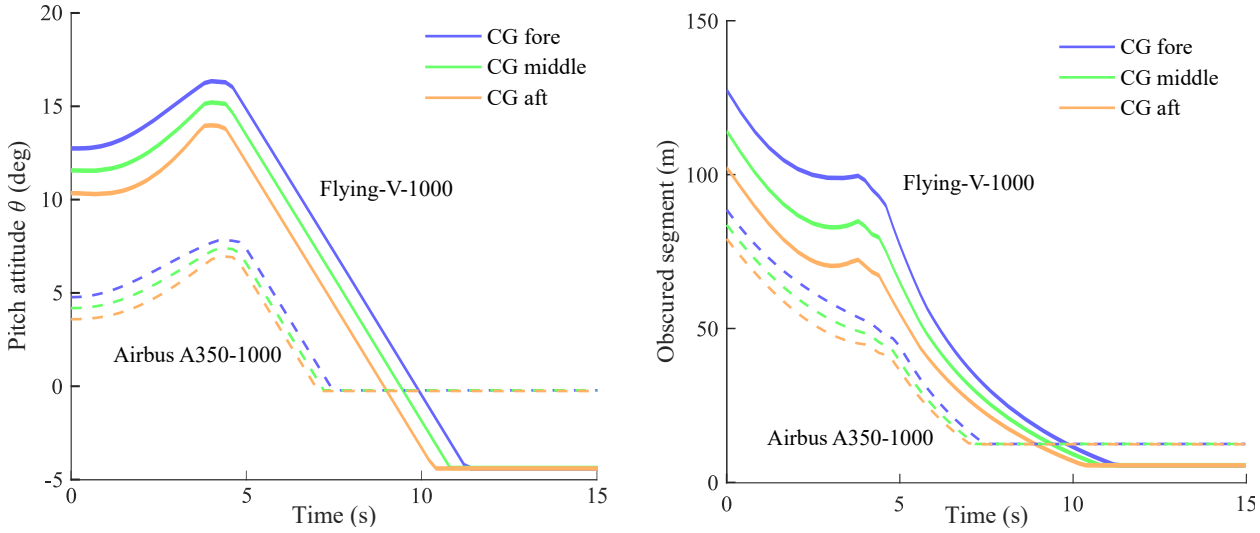

a) Pitch attitude angle

b) Obscured segment

Fig. 13 Time histories comparison of pitch angle and obscured segment on the runway during landing, for different positions of the CG.

Flying-V-1000 can be up to twice as large as the one of the A350-1000, depending on the CG position.

C. Climb performance

Quasi-steady climb performance are calculated by trimming the aircraft at various points in the airspeed-altitude plane. The aircraft is assumed to be in MTOM conditions, with the CG at its forward limit position. A throttle input of 85% is imposed, to simulate the maximum continuous thrust available during climb and cruise operations [15, 36].

Figure 14 compares the maximum Angle of Climb (AoC) of both aircraft in the h–V flight envelope, and Figure 15 shows a similar comparison for the Rate of Climb (RoC). The solid black line highlights the locus of maximum values of the respective flight parameters, hence providing the steepest and fastest climb trajectories, respectively. The drag divergence Mach number M_{dd} and the speed of sound are also drawn.

Both the AoC and RoC contours are comparable for the two aircraft. The Flying-V achieves its steepest climb trajectory at a slightly lower airspeed than the A350, on average, while the two fastest climb trajectories are basically

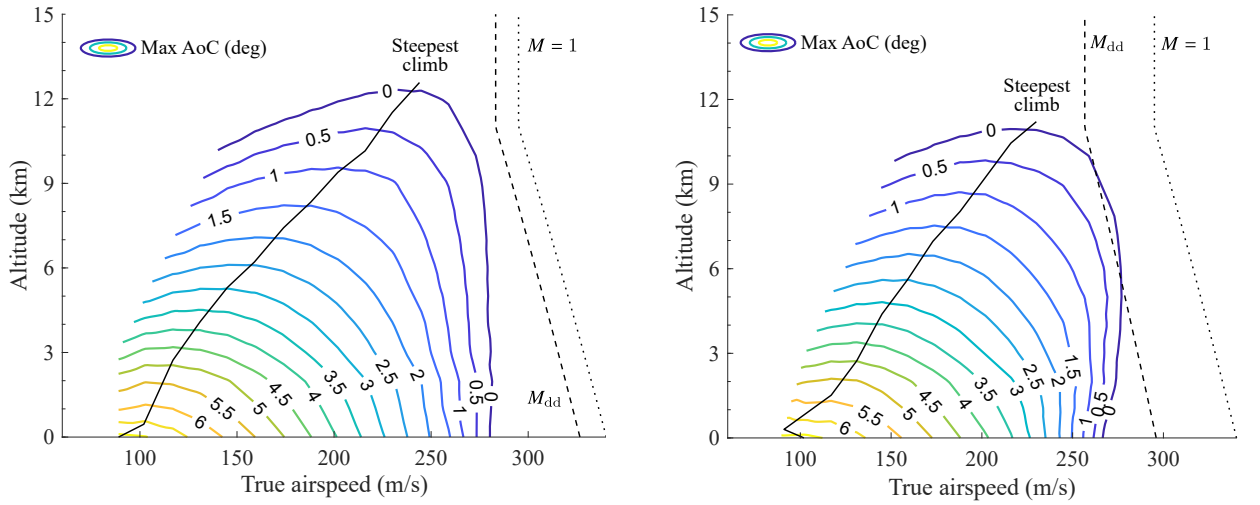

a) Flying-V-1000

b) Airbus A350-1000

Fig. 14 Maximum steady Angle of Climb (AoC) comparison in the h–V flight envelope, for maximum continuous thrust and MTOM.

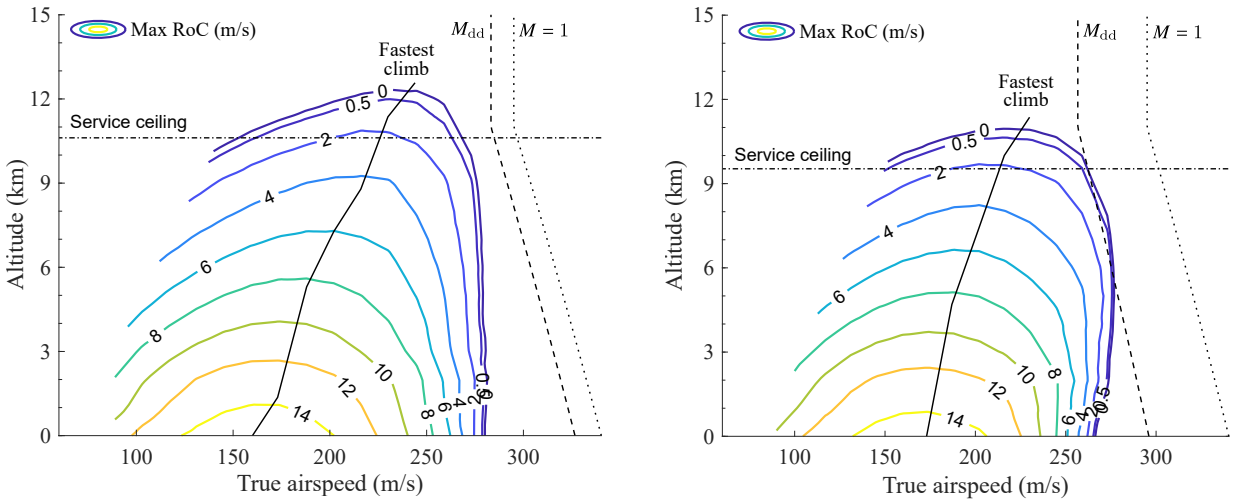

a) Flying-V-1000 **b)** Airbus A350-1000

Fig. 15 Maximum steady Rate of Climb (RoC) comparison in the h–V flight envelope, for maximum continuous thrust and MTOM.

overlapping. Moreover, the Flying-V achieves a greater AoC and a higher RoC for every feasible combination of altitude and speed. Since the two aircraft have the same T/W ratio, such performance advantage is due to its higher aerodynamic efficiency [2].

These results also enable the Flying-V to achieve a higher service and absolute ceiling altitudes, h_{serv} and h_{abs}, than the A350. The service ceiling has been calculated as the highest altitude where an aircraft can climb at a rate of 100 ft/min $\approx$ 0.5 m/s at maximum continuous thrust, and is reported also in Figure 15. The absolute ceiling has been computed as the highest altitude achievable at maximum available thrust ($\delta_T = 1$) with zero residual RoC. The service and absolute ceiling altitudes are reported in Table 5.

Table 5 Service and absolute ceiling altitudes comparison at MTOM, forward-limit CG position.

	Throttle setting	Flying-V-1000	Airbus A350-1000
h_{serv}	$\delta_T = 0.85$	12.0 km	10.6 km
h_{abs}	$\delta_T = 1.00$	13.3 km	12.0 km

Lastly, Figure 16 shows the AoC achieved at speed V_2, with OEI, landing gear retracted, and maximum thrust ($\delta_T = 1$) for both aircraft in take-off configuration. Certification specification CS25.121 dictates that a two-engined aircraft should be able to achieve a steady AoC of 1.37 deg in such conditions [32], and this limit is also reported in the chart. The Flying-V achieves the required climb angle for all tested altitudes and mass fractions, while the A350 meets the requirement for all but the most extreme case. Additionally, the Flying-V always achieves a larger AoC than the A350, which decreases with increasing mass fraction and altitude.

D. Cruise performance

For the evaluation of cruise performance, each aircraft is trimmed at the nodes of a pre-defined grid in the h–V flight envelope, in steady level flight and at MTOM. The relevant parameters are then extracted to calculate performance metrics in trimmed flight conditions. With this approach, only instantaneous cruise performance is analyzed in the present work.

The maximum values of the aerodynamic efficiency L/D, transonic efficiency ML/D, and Range Parameter RP are compared for the two aircraft in Table 6, together with the corresponding Mach number and lift coefficient. Contour plots of the RP as a function of the Mach number and the lift coefficient are shown in Figure 17.

The maximum trimmed L/D of the Flying-V-1000 is 17% higher than the one of the A350-1000. For both aircraft, the maximum trimmed L/D is located at a smaller Mach number than the assumed cruise value of $M = 0.85$. This is

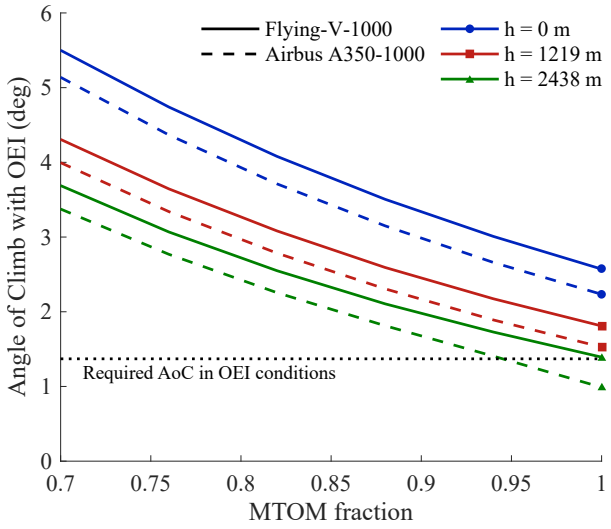

Fig. 16 Climb angle comparison in steady One Engine Inoperative (OEI) conditions, $V = V_2$, $\delta_T = 1$, landing gear retracted.

most likely due to the implemented transonic wave drag model (Table 3b). The maximum transonic efficiency ML/D of the Flying-V-1000 is 21% higher than the one of the A350. Contrarily to the previous case, the maximum values of the transonic efficiency occur at similar Mach numbers for both aircraft. When the least simplified metric is used, these results are confirmed. The Flying-V-1000 achieves a maximum trimmed Range Parameter RP 21% higher than its competitor. When compared to the maximum ML/D, the maximum RP occurs in the same flight conditions for the Flying-V, while it occurs at lower Mach number and higher C_L for the A350. This is also suspected to be due to the model used for the drag-divergence Mach number.

If both aircraft were to fly at the Mach number and lift coefficient that maximize RP with a mass equal to the MTOM, this would yield a cruise altitude of 12.0 km for the Flying-V and 11.3 km for the A350. For the Flying-V, this is the same altitude as its service ceiling. For the A350, such cruise altitude would be higher than its service ceiling, but lower than its absolute ceiling at MTOM.

A more operational visualization of cruise performance is presented in the so-called "cruise grid" of Figure 18. This chart shows that the cruise performance of the Flying-V remains vastly superior even when aircraft and fuel weight is explicitly brought into the performance metrics. For the same mass fraction, the SAR of the Flying-V is significantly greater than the one of the A350 at all Mach numbers relevant for cruise flight. Moreover, the SAR of the Flying-V at MTOM is greater than the one of the A350 with mass fractions higher than 0.7 for $M >= 0.68$. On the other hand, the Flying-V achieves its maximum SAR at lower Mach numbers (on average) than the A350, for the same mass fraction. Also, the cruise grid of the A350 appears to be flatter around the maximum than the one of the Flying-V, especially for higher Mach numbers. This is important, as it allows the A350 to operate at cruise speeds higher than the optimal one, while sacrificing only a small percentage of Specific Air Range. The SAR performance of the Flying-V seems to decrease very rapidly as the Mach number increases towards the high transonic regime. This is surprising in light of the very high drag-divergence Mach number predicted by the compressibility model used for this specific study, and demands further investigation.

Table 6 Comparison of maximum cruise performance metrics in trimmed level flight at MTOM.

Perf. metric Φ	Flying-V-1000			Airbus A350-1000		
	Φ	$M_{\|\Phi}$	$C_{L\|\Phi}$	Φ	$M_{\|\Phi}$	$C_{L\|\Phi}$
$(L/D)^{\text{tr}}_{\text{max}}$	23.7	0.75	0.37	20.3	0.65	0.71
$(ML/D)^{\text{tr}}_{\text{max}}$	18.9	0.82	0.32	15.6	0.83	0.53
$RP^{\text{tr}}_{\text{max}}$	9.7	0.82	0.32	8.0	0.75	0.69

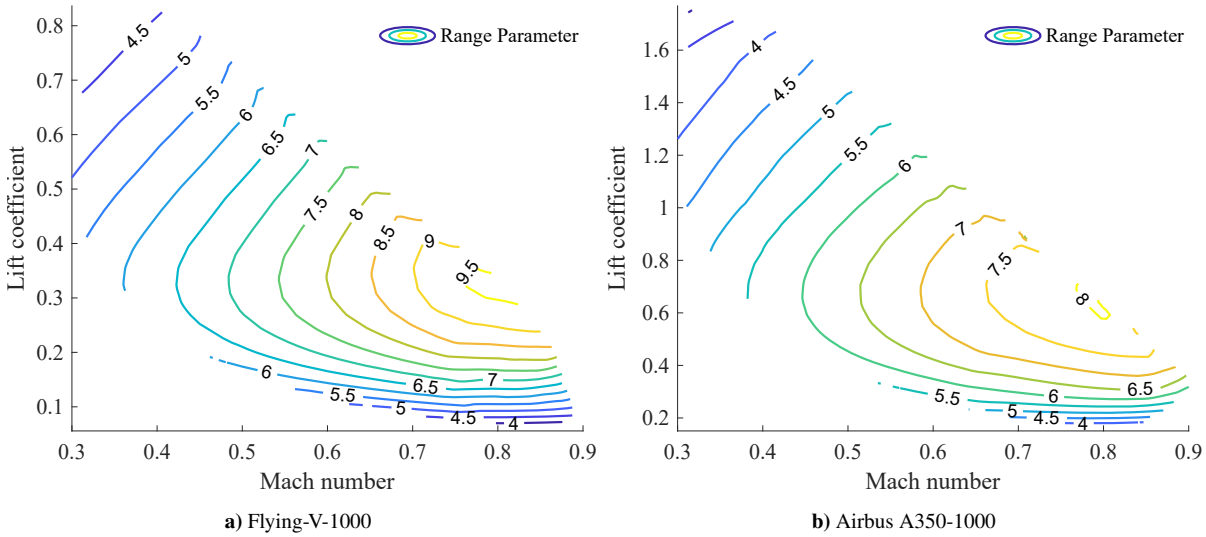

a) Flying-V-1000 **b)** Airbus A350-1000

Fig. 17 Contour plots of the Range Parameter *RP* as a function of lift coefficient and flight Mach number, in trimmed level flight at MTOM.

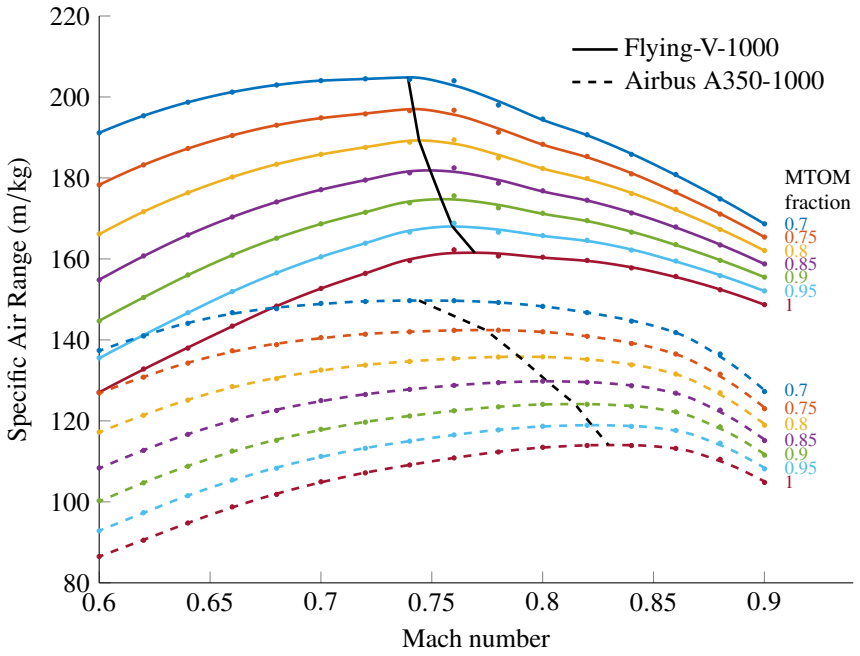

Fig. 18 Cruise grid comparing the Specific Air Range (*SAR*) of the Flying-V-1000 and the Airbus A350-1000 for different fractions of their respective MTOM, in trimmed conditions at $h = 11$ km.

VI. Conclusions

This paper has presented an evaluation of the flight performance characteristics of the Flying-V-1000 and a comparison to the ones of its envisioned competitor, the Airbus A350-1000. Identical thrust-to-weight ratios have been assumed for both aircraft. Classic performance metrics related to the take-off, landing, climb and cruise mission phases have been evaluated by means of a simple flight simulation framework.

On average, the Flying-V-1000 features a 25% shorter take-off distance and 30% shorter Balanced Field Length (BFL) than the A350-1000. The first difference can mainly be attributed to the larger tail-strike pitch attitude of the Flying-V, which results in significantly lower unstick and rotation speeds. The second difference is mainly due to the superior breaking performance, due to a better relative placement of control surfaces and main landing gear.

Both aircraft have similar approach speeds and landing field lengths. Due to its highly swept wing, the Flying-V

approaches and touches down at a significantly larger pitch angle, leading to an increased de-rotation distance. On the other hand, the Flying-V has a shorter ground run thant the A350 thanks to the nose-down attitude when on the ground and to the aforementioned superior braking performance. Due to the large pitch angle at approach, the obscured segment of the pilot's vision during landing is considerably larger for the Flying-V than for the A350. This could become problematic during operations, and requires further investigation.

Due to the higher maximum aerodynamic efficiency, the Flying-V outperforms the A350 in terms of climbing performance. This is reflected in a higher service ceiling and absolute service ceiling, and slightly better compliance with certification requirements for One Engine Inoperative (OEI) climb conditions.

The evaluation of the *SAR* has shown that the Flying-V-1000 outperforms the A350-1000 in terms of cruise efficiency at basically all mass fractions and relevant Mach numbers. This result also stems from the 17% higher maximum L/D ratio for the Flying-V, as well as from its 10.8% higher drag divergence Mach number with respect to the A350.

It can be concluded that the Flying-V-1000 outperforms the A350-1000 model in terms of take-off, climb and cruise performance for an identical thrust-to-weight ratio. The landing distances of the two aircraft are comparable, although the significantly larger obscured segment of the pilot's vision could cause problems for the Flying-V during landing with poor visibility.

Further research could consider multi-body dynamics simulation for a precise analysis of the loads on the landing gear during take-off and landing operations. In a similar way, locally or globally optimal mission simulation would be advised to validate the instantaneous performance obtained for the climb and descent phases. Lastly, it would be beneficial to increase the fidelity of the aerodynamic model, by means of using 3D panel methods and/or more sophisticated models for compressibility and ground effect.

References

[1] Martinez-Val, R., Perez, E., Puertas, J., and Roa, J., "Optimization of planform and cruise conditions of a transport flying wing," *Proceedings of the Institution of Mechanical Engineers, Part G: Journal of Aerospace Engineering*, Vol. 224, No. 12, 2010, pp. 1243–1251. https://doi.org/10.1243/09544100jaero812.

[2] Faggiano, F., Vos, R., Baan, M., and Van Dijk, R., "Aerodynamic design of a Flying-V aircraft," *17th AIAA Aviation Technology, Integration, and Operations Conference: 5-9 June 2017, Denver, Colorado [AIAA 2017-3589] AIAA*, 2017. https://doi.org/10.2514/6.2017-3589.

[3] Airbus S.A.S., "Global Market Forecast 2019 – 2038," techreport, Blagnac, France, 2019. URL https://www.airbus.com/aircraft/market/global-market-forecast.html.

[4] Benad, J., "The Flying V A new Aircraft Configuration for Commercial Passenger Transport," 2015. https://doi.org/10.25967/370094.

[5] Oosterom, W., and Vos, R., "Conceptual Design of a Flying-V Aircraft Family," *AIAA AVIATION 2022 Forum*, American Institute of Aeronautics and Astronautics, 2022. https://doi.org/10.2514/6.2022-3200.

[6] Claeys, M. B. P., "Flying V and Reference Aircraft Structural Analysis and Mass Comparison," Msc thesis, Delft University of Technology, 2018. URL http://resolver.tudelft.nl/uuid:ee7f2ecb-cdb6-46de-8b57-d55b89f8c7e6.

[7] Palermo, M., and Vos, R., "Experimental Aerodynamic Analysis of a 4.6%-Scale Flying-V Subsonic Transport," *AIAA Scitech 2020 Forum*, American Institute of Aeronautics and Astronautics, 2020. https://doi.org/10.2514/6.2020-2228.

[8] Viet, R., "Analysis of the flight characteristics of a highly swept cranked flying wing by means of an experimental test," Msc thesis, Delft University of Technology, 2019. URL http://resolver.tudelft.nl/uuid:90de4d9e-70ae-4efc-bd0a-7426a0a669c3.

[9] Ruiz Garcia, A., Vos, R., and de Visser, C., "Aerodynamic Model Identification of the Flying V from Wind Tunnel Data," *AIAA AVIATION 2020 FORUM*, American Institute of Aeronautics and Astronautics, 2020. https://doi.org/10.2514/6.2020-2739.

[10] Ruiz Garcia, A., Brown, M., Atherstone, D., v. Arnhem, N., and Vos, R., "Aerodynamic Model Identification of the Flying V from Sub-Scale Flight Test Data," *AIAA SCITECH 2022 Forum*, American Institute of Aeronautics and Astronautics, 2022. https://doi.org/10.2514/6.2022-0713.

[11] Cappuyns, T., "Handling Qualities of a Flying V Configuration," Msc thesis, Delft University of Technology, 2019. URL http://resolver.tudelft.nl/uuid:69b56494-0731-487a-8e57-cec397452002.

[12] Vugts, G., Stroosma, O., Vos, R., and Mulder, M., "Evaluation of Flightpath-oriented Control Allocation for the Flying-V," 2023.

[13] Joosten, S., Stroosma, O., Vos, R., and Mulder, M., "Simulator Assessment of the Lateral-Directional Handling Qualities of the Flying-V," *Proceedings of AIAA SciTech*, 2023.

[14] Airbus S.A.S., "A350 Aircraft Characteristics and Maintenance Planning, Revision No. 10," Tech. rep., 2022. URL https://www.airbus.com/sites/g/files/jlcbta136/files/2022-05/Airbus-Commercial-Aircraft-AC-A350-900-1000.pdf.

[15] European Aviation Safety Agency, "Type-Certificate Data Sheet: Trent XWB series engines," Tech. rep., 2019. URL https://www.easa.europa.eu/sites/default/files/dfu/EASAE111TCDSissue12_TrentXWB.pdf.

[16] Bourget, G., "The effect of landing gear implementation on Flying V aerodynamics, stability and controllability," Msc thesis, Delft University of Technology, 2020. URL http://resolver.tudelft.nl/uuid:599eca91-6200-4d29-8dd7-e4e7060703e1.

[17] Raymer, D. P., *Aircraft design: a conceptual approach*, 5th ed., American Institute of Aeronautics and Astronautics, 2012.

[18] Torenbeek, E., *Synthesis of Subsonic Aircraft Design*, Delft University Press, 1988.

[19] Feagin, R., and W., M., "Delta Method, An Empirical Drag Buildup Technique," Tech. rep., 1978. URL https://ntrs.nasa.gov/citations/19790009630.

[20] Vargas-Jimenez, J. A., and Vos, R., "Development of a Wave Drag Prediction Method for the Conceptual Design Phase," *54th AIAA Aerospace Sciences Meeting*, American Institute of Aeronautics and Astronautics, 2016. https://doi.org/10.2514/6.2016-1279.

[21] Erdincler, O., "Aerodynamic and Performance Analysis of Ground Spoilers on the Flying V," Msc thesis, Delft University of Technology, 2021. URL http://resolver.tudelft.nl/uuid:d8176c14-f3e1-4a6a-99b0-55c7251f9762.

[22] Rubio Pascual, B., and Vos, R., "The Effect of Engine Location on the Aerodynamic Efficiency of a Flying-V Aircraft," *AIAA Scitech 2020 Forum*, American Institute of Aeronautics and Astronautics, 2020. https://doi.org/10.2514/6.2020-1954.

[23] Bartel, M., and Young, T., "Simplified Thrust and Fuel Consumption Models for Modern Two-Shaft Turbofan Engines," *Journal of Aircraft*, Vol. 45, No. 4, 2008, pp. 1450–1456. https://doi.org/10.2514/1.35589.

[24] Jenkinson, L., Simpkin, P., and Rhodes, D., *Civil Jet Aircraft Design*, American Institute of Aeronautics and Astronautics, Inc., 1999. https://doi.org/10.2514/4.473500.

[25] Torenbeek, E., "Optimum Cruise Performance of Subsonic Transport Aircraft," Tech. rep., Delft University of technology, Delft, 1995. URL http://resolver.tudelft.nl/uuid:8be05c68-1826-4809-b8c0-de37eb7df469.

[26] Ruijgrok, G. J. J., *Elements of Airplane Performance*, 2nd ed., Delft Academic Press (VSSD), Delft, 2009.

[27] van Ginneken, D., Voskuijl, M., van Tooren, M., and Frediani, A., "Automated Control Surface Design and Sizing for the Prandtl Plane," *51st AIAA/ASME/ASCE/AHS/ASC Structures, Structural Dynamics, and Materials Conference*, American Institute of Aeronautics and Astronautics, 2010. https://doi.org/10.2514/6.2010-3060.

[28] Voskuijl, M., de Klerk, J., and van Ginneken, D., "Flight Mechanics Modeling of the PrandtlPlane for Conceptual and Preliminary Design," *Optimization and Its Applications*, Springer US, 2012, pp. 435–462. https://doi.org/10.1007/978-1-4614-2435-2_19.

[29] Varriale, C., Hameeteman, K., Voskuijl, M., and Veldhuis, L. L. M., "A Thrust-Elevator Interaction Criterion for Aircraft Optimal Longitudinal Control," *AIAA Aviation Forum*, American Institute of Aeronautics and Astronautics, 2019. https://doi.org/10.2514/6.2019-3001.

[30] Varriale, C., and Voskuijl, M., "A Control Allocation approach to induce the center of pressure position and shape the aircraft transient response," *Aerospace Science and Technology*, Vol. 119, 2021. https://doi.org/10.1016/j.ast.2021.107092.

[31] Varriale, C., and Voskuijl, M., "A trim problem formulation for maximum control authority using the Attainable Moment Set geometry," *CEAS Aeronautical Journal*, 2021. https://doi.org/10.1007/s13272-021-00560-4.

[32] European Aviation Safety Agency, *Certification Specifications for Large Aeroplanes CS-25A19*, EASA, 2017. URL https://www.easa.europa.eu/en/document-library/certification-specifications/cs-25-amendment-19.

[33] Vos, R., Eeckels, C., Schoustra, R.-J., and Voskuijl, M., "Analysis of a Ground-Based Magnetic Propulsion System," *Journal of Aircraft*, Vol. 51, No. 3, 2014, pp. 1013–1022. https://doi.org/10.2514/1.c032555.

[34] Federal Aviation Administration, *Federal Aviation Regulations*, United States Department of Transportation, 2022. URL https://www.ecfr.gov/current/title-14/chapter-I/subchapter-G/part-135/appendix-AppendixAtoPart135.

[35] Airbus S.A.S., "A330 Flight Deck and Systems Briefing For Pilots," Tech. rep., 2015.

[36] Scholz, D., "Skript zur Vorlesung Flugzeugentwurf, Anhang C," , 1999. URL https://www.fzt.haw-hamburg.de/pers/Scholz/Flugzeugentwurf.html.